

# The two-phase flow at gas-evolving electrodes: Bubble-driven and Lorentz-force-driven convection

T. Weier<sup>a</sup> and S. Landgraf

Institute of Fluid Dynamics, Helmholtz-Zentrum Dresden-Rossendorf, Bautzner Landstr.  
400, 01328 Dresden, Germany

Received 17 December 2012 / Received in final form 5 February 2013  
Published online 26 March 2013

**Abstract.** We observe electrolysis with gas evolution, a phenomenon occurring in a number of industrial scale electrochemical processes. Here, water electrolysis takes place in a small undivided electrolysis cell consisting of vertical electrodes embedded in a larger glass vessel which contains a dilute NaOH solution. Fluid flow velocities are measured by particle image velocimetry with fluorescent tracers, while size distribution and velocities of the bubbles are determined from bubble shadow images obtained with a high speed camera. Coalescence phenomena are observed in the flow and explain the relatively wide distribution of bubble sizes. Depending on the gap width and the current density, bubbles ascending near the electrodes form two discernible bubble curtains (low average void fraction, wide gaps) or a flow profile more akin to a channel flow (high average void fraction, small gaps). If the flow consists of separate bubble curtains, instabilities develop not unlike to those of a single phase wall jet. Finally, the influence of different wall parallel Lorentz force configurations on the velocity distribution in the cell is investigated. These Lorentz forces are generated by permanent magnets mounted behind the electrodes. Depending on gap width, current density, and magnet configuration, liquid phase velocities can be increased by several times compared to the baseline case.

## 1 Introduction

Research on water electrolysis roughly follows the long-term oil prices with a certain time lag. At present, we experience increased research activities which receive an additional boost from the transformation of the German electrical energy infrastructure from mainly fossil and nuclear to renewable sources (energy transition). Switching to volatile sources and supplying the energy demands at the same time generates a need for huge storage capacities. Hydrogen is one of the prime candidates for direct long term storage and a base material for methanation (power-to-gas). Presently, a typical efficiency of 60% [1] makes the electrolyzer a weak link in the efficiency chain. In the long term, an increase in the electrolyzer efficiency to 90% is envisioned [2].

<sup>a</sup> e-mail: [t.weier@hzdr.de](mailto:t.weier@hzdr.de)

Power losses in alkaline water electrolysis result from the decomposition voltage dictated by thermodynamics, overvoltages and ohmic potential drops in the electrodes, the diaphragm or membrane, and the electrolyte. Especially for higher current densities, a large part of the cell resistance is due to electrolytically generated bubbles [3,4]. Since the bubbles act as dispersed insulators, they reduce the effective conductivity of the electrolyte [5]. A number of equations have been suggested since the seminal work of Maxwell [6] to describe the effective resistivity of monodisperse and polydisperse distributions of non-conducting spheres in a conducting liquid at low void fractions, see, e.g., [7]. Differences between the various expressions are minor. Overall, they predict a slightly larger than proportional decrease of the normalized effective conductivity with the void fraction. Therefore, in order to minimize power losses, the void fraction in the electrode gap should be as small as possible. To decrease voidage, expanded metal [8] or perforated plate [9] electrodes are used, which allow the bubbles to leave the interelectrode gap and move to the electrode's back side. More sophisticated electrode shapes serving the same purpose have been investigated by, e.g., [10–14], sometimes in the context of chlor-alkali electrolysis.

It was realized relatively early that forced convection too is able to reduce void fraction, electrode bubble coverage, and hence cell resistance [3,4,15–18]. Commonly, only a minor change in the cell resistance is found for very mild forced convection, while above a certain liquid velocity, the effective conductivity of the electrolyte solution increases more rapidly with flow speed.

Especially in the earlier studies, the fluid flow in the cells was characterized by its mean value only, and detailed studies of the velocity distribution in the cells have seldom been reported. This situation is changing, but detailed experimental studies on fluid dynamics in gas evolving electrolysis cells are still relatively scarce. Kuhn and Kreysa [19] report the time averaged liquid flow field at flat plate and “Venetian blind” electrodes measured by laser Doppler anemometry (LDA). Fukunaka et al. [20] extracted bubble velocities from cinematographic films in a probably labor-intensive process. Boissonneau and Byrne [21] performed LDA and particle image velocimetry (PIV) measurements in a small flow-through cell immersed in a larger reservoir. Kuroda et al. [22] report on liquid flow fields measured by PIV and particle tracking velocimetry (PTV) and bubble velocities determined by PIV.

If the void fraction is not too large, the bubble distribution and the bubble traces can be used to visualize the flow and give a qualitative picture of the velocity distribution. In this way, the appearance of a recirculation region under certain conditions has been observed by Sigrist [23] and later Riegel et al. [24]. Vogt [25,26] explained the recirculation as to be rooted in an instability.

An increasing number of publications are dedicated to numerical investigations of electrolysis cells. Dahlkild [27] simulated the boundary layer on a single vertical gas evolving electrode by solving the boundary layer equations using a finite difference method. The local current densities he found were in good agreement with the experimental values reported by Hine and Murakami [4]. The codes applied in the references discussed in the following are all based on finite volumes. Mat et al. [28–30] used PHOENICS to simulate the two-phase flow in different gas evolving electrochemical cells with an Euler-Euler strategy, accounting for the turbulent liquid phase with a  $k-\varepsilon$  model. FLUENT was applied by Mandin et al. [31] to calculate the flow in a cell with a single vertical gas evolving electrode. Alexiadis and co-workers published a number of papers on two-phase flow simulations in different electrochemical cells [32,33] based on Euler-Euler-simulations with OpenFOAM. They found transition to a so called “pseudo-turbulent” flow in a narrow vertical channel with gas evolution on one side [32] if the current density is high and a sufficient amount of small bubbles is present. In [34] a dimensionless group for the transition criterion from laminar to “pseudo-turbulent” flow is given and discussed in connection with the linear stability

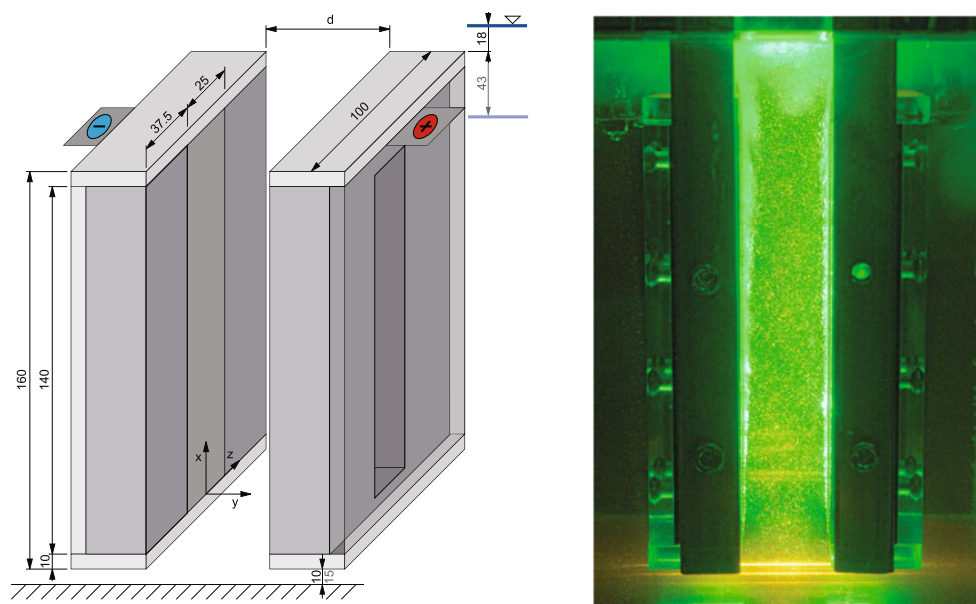


**Fig. 1.** Experimental setup, dimensions in mm (left). Dimmed colors: electrode protrudes the water surface. Photograph of the operational cell with light sheet (right).

analysis of a simplified flow profile. It turned out that the stability properties of the flow in single cells are quite different from those of the flow in multiple interconnected cells [33].

The influence of magnetic fields on the flow in gas evolving cells has recently been a topic of considerable interest [35–41]. Most of the papers observed a reduced Ohmic resistance of the cell and relate this to Lorentz force driven convection and thereby accelerated removal of bubbles from the interelectrode gap. The typical setup in these settings are electric and magnetic fields which are perpendicular in a first approximation. A different configuration has been investigated by Koza and co-workers and Fernández et al. [42–45], where magnetic and electric fields are mainly parallel in most of the cell volume. However, a bubble on the electrode acts as an insulator and therefore causes a distortion of the current density distribution. This gives rise to a Lorentz force in the vicinity of the bubble, driving a rotational flow. While Koza et al. [42–44] observed reduced bubble departure diameters and decreased bubble coverage of the electrode with magnetic field, Fernández et al. [45] found that a bubble on a micro-electrode grows to larger diameters when a magnetic field is applied. At the moment, it is safe to say that not all effects of magnetic fields on electrolytic bubbles are sufficiently understood.

## 2 Setup

Two stainless steel (1.4301) electrodes were embedded in plastic holders made from PVC and PMMA as sketched in the left part of Fig. 1. Yokes connect the holders to a manual traverse, allowing for easy adjustment of the electrode gap. The whole arrangement was placed in the center of a glass vessel ( $200 \times 170 \times 200 \text{ mm}^3$ ) filled with a 0.25 M NaOH solution. A fixed current from a current regulated power supply fed the electrodes while two multimeters monitored the total current and the cell voltage.

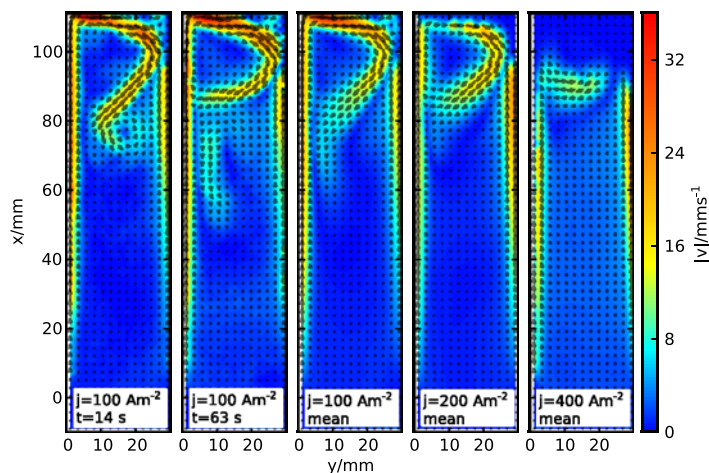
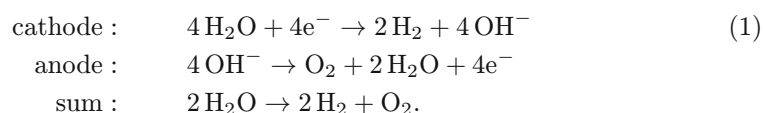


**Fig. 2.** Flow field for the surface protruding electrodes and different current densities.

The PIV setup consists of a 250 mW diode pumped solid state laser (532 nm) with light sheet optics and a Photron Fastcam 1024PCI 100K camera with a long pass filter in front of the lens. The light sheet entered the glass vessel through the base plate and goes through the origin of the coordinate system (Fig. 1). Fluorescent particles FPP-RhB-35 from Dantec Dynamics GmbH have been used for seeding. Combining fluorescent particles and a long pass filter allows for measurement of the liquid velocity without distortions from the laser light reflected by the bubbles. The latter is blocked by the filter and therefore not recorded by the camera. About 6400 images were recorded for each configuration. While the image height was always 1024 pixels and covered most of the electrode, the image width has been adjusted roughly to the electrode gap width and was either 256 or 128 pixels. Most of the images have been captured with a frequency of 60 Hz. They were evaluated in sequence with PIVview2C from PivTec using multigrid interrogation with image deformation and a final window size of  $16 \times 16$  pixels and 50% overlap. These results were used in most of the cases as predictors for a subsequent PTV evaluation of the data. Bubble images have been taken in extra runs with back-illumination.

When current is applied to the electrodes, in the alkaline environment of the NaOH electrolyte the reactions take place (see, e.g., [46]):



## 3 Results

### 3.1 Baseline flow

#### 3.1.1 Influence of the electrolyte level

The flow in the upper part of the cell is mainly determined by the electrolyte level, i.e. the conditions at the top of the electrode. If the liquid level is low and the electrodes protrude the electrolyte surface, a large recirculation region below the liquid-gas interface is formed as shown in Fig. 2. This has been observed already in

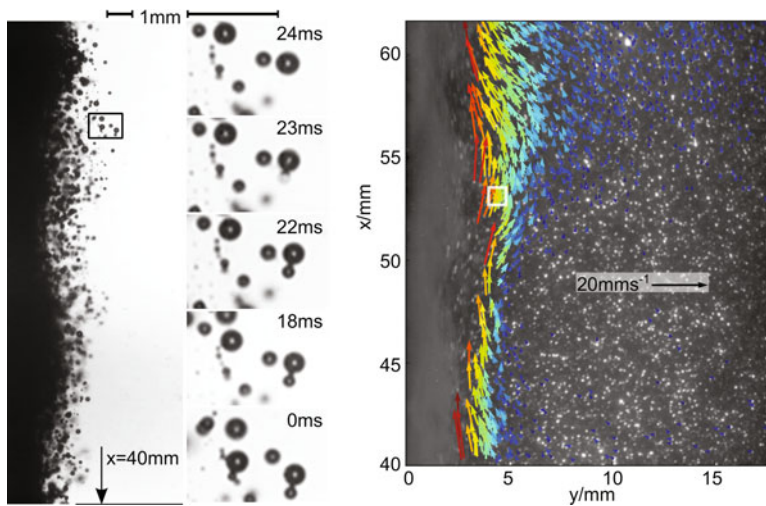


**Fig. 3.** H<sub>2</sub> bubble curtain near the cathode and zoomed sequence (black rectangle) of coalescing bubbles (left,  $j = 1430 \text{ Am}^{-2}$ ). Snapshot of the liquid velocity distribution near the bubble curtain (right,  $j = 800 \text{ Am}^{-2}$ ).  $d = 30 \text{ mm}$  for both cases.

the experiments of Shah and Jorne [47] and by numerical investigations [29,33,48]. Corresponding to the sketch in Fig. 1, H<sub>2</sub> is developed on the left and O<sub>2</sub> on the right hand side. According to Eq. (1), the volume of the generated hydrogen is twice as large as that of oxygen. As a consequence, liquid momentum on the cathodic side of the cell is higher than on the anodic side, and the deflection of the liquid motion on the free surface leads to a clockwise circulation. While most of the larger bubbles are able to penetrate the liquid-gas interface, smaller ones remain in the fluid and revolve with the liquid flow. As can be seen from the two leftmost contour plots in Fig. 2 showing snapshots of the liquid velocity distribution taken at 14 s and 63 s after the start of the measurement, the flow is instationary. The extent of the recirculation region in the time averaged flow field (central plot in Fig. 2) is between the two positions shown in the snapshots. The two rightmost plots in Fig. 2 show the flow field for increased current densities of  $j = 200 \text{ A/m}^2$  and  $400 \text{ A/m}^2$ . While increased liquid phase velocities can be observed in the bubble curtain at the anodic side, this expected behavior is not visible on the cathodic side. A seemingly stagnant region appears near the surface for  $j = 200 \text{ A/m}^2$  and grows to considerable size at  $400 \text{ A/m}^2$ . However, these findings do not reflect the real liquid flow field, but are due to the bubble induced increase in the solutions optical density. The void fractions in the cathodic bubble curtain and in the top part of the cell become so high that the fluorescent light emitted by the tracer particles is blocked, and the camera is unable to receive information from these regions. All experiments described in the following have been performed with completely submerged electrodes. In this configuration, the direction of the flow in the electrode gap is always upwards, and no recirculation region appears.

### 3.1.2 Liquid phase velocities and bubble characteristics near the cathode

A shadowgraph of the bubble distribution in the vicinity of the cathode is shown in the left part of Fig. 3 for a electrode gap of  $d = 30 \text{ mm}$  and a current density of  $j = 1430 \text{ Am}^{-2}$ . Void fraction in the bubble curtain is so high that the back-illumination



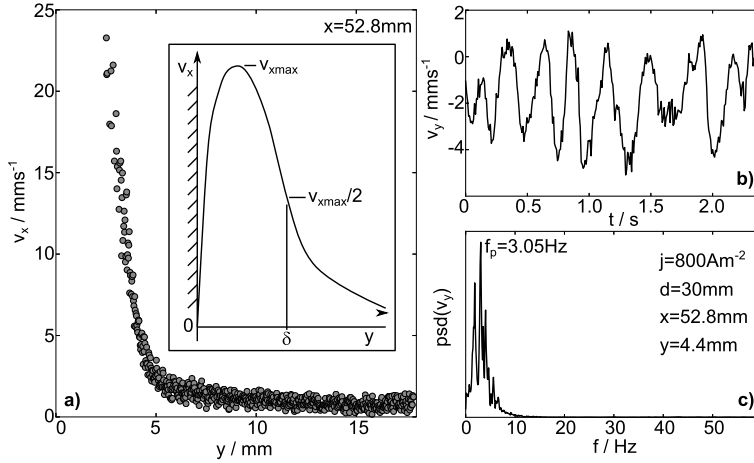


**Fig. 4.** a) Time averaged velocity in  $x$ -direction vs. wall distance with sketch of a wall jet (insert). b) Time dependent wall normal velocity and c) its power spectral density. Parameters and positions as annotated.

is completely absorbed. This way, only the boundary of the bubble curtain and a few dispersed bubbles traveling upstream in a region farther from the cathode are detectable. For this large electrode gap, the flow in the bulk is practically stagnant, and motion is limited to the natural convection boundary layers at the electrodes. The bottom of the image is  $x = 40 \text{ mm}$  above the electrode's leading edge, i.e. the origin of ordinates. In a sequence taken from the enlarged part of the image enclosed in the black rectangle, coalescence of two bubbles can be observed. 0 ms denotes the time corresponding to the full image, coalescence takes place between 22 ms and 23 ms and is too fast to be completely resolved with the 1 kHz frame rate of the camera. However, a light gray footprint of the smaller bubble is still visible at 23 ms.

**The boundary of the bubble curtain is wavy.** This has already been observed in the visualizations of Boissonneau and Byrne [21] for comparable current densities and positions as well as by Aldas et al. [30]. Liquid phase velocities shown in the right part of Fig. 3 mirror the waviness of the bubble curtain. The latter manifests itself as the grayish area on the left of the PIV record. The time dependent wall normal velocity component  $v_y$  averaged over the small white square with 0.85 mm long edges centered at  $x = 52.8 \text{ mm}$  and  $y = 4.4 \text{ mm}$  is given in Fig. 4b. The power spectral density (psd, Fig. 4c) of  $v_y$  shows a peak at 3.05 Hz. Since the bubble curtain entrains fluid the mean value of  $v_y$  is less than zero. Figure 4a gives a plot of the time averaged electrode parallel velocity component  $v_x$  versus the distance from the electrode  $y$  at  $x = 52.8 \text{ mm}$ . While optical access to the immediate vicinity of the wall is blocked, a steep gradient towards higher velocities from the almost stagnant bulk fluid can be observed for  $y < 5 \text{ mm}$ . Due to the no-slip condition at the wall, a velocity maximum  $v_{x\max}$  has to occur for  $y < 2.5 \text{ mm}$ . Therefore, we expect a flow profile similar to that of a wall jet as sketched in the inset of Fig. 4a. Even if the bubble driven flow observed here differs in many aspects from a canonical wall jet, it is tempting to compare the stability characteristics of both cases. Doing so, we find that the peak frequency of the  $v_y$  fluctuations should fit reasonably into the range of the most amplified frequencies for a wall jet as reported e.g. in [49]. A quantitative comparison is made impossible by the lack of information about  $v_{x\max}$  and consequently the jet's half width  $\delta$ .

Velocities and sizes of the dispersed bubbles are collected in Fig. 5. Usually, hydrogen bubbles generated electrolytically in an alkaline environment are relatively

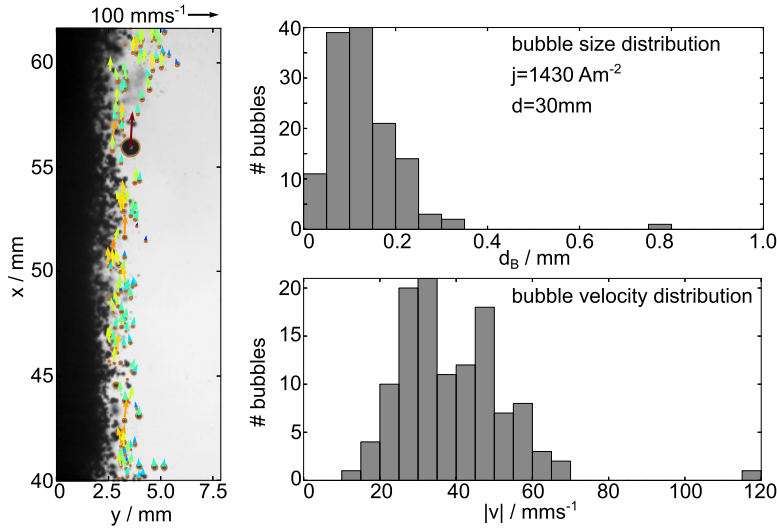


**Fig. 5.** Dispersed bubbles in front of the bubble curtain, detected bubbles tagged and velocity vectors added (left). Right: bubble size and velocity distributions. Parameters as annotated.

small with typical diameters around and below  $50\ \mu\text{m}$  [50]. The larger mean diameter observed here can be explained by taking into account that only bubbles relatively far from the electrode were detectable and could be used for the statistics. These bubbles must have been passed the bubble curtain where they had a high probability of collision and coalescence with other bubbles. The bubble velocity distribution is considerably broader than the bubble size distribution because the counted bubbles ascend in a region with a steep gradient in the mean liquid velocity. However, since the liquid and bubble velocities could not be determined simultaneously with the current setup, no correction of the bubble velocities has been attempted.

### 3.2 Lorentz force influence

Notches in the PVC blocks containing the electrodes (see Fig. 1) allow for the placement of permanent magnets directly behind the 0.5 mm thick electrodes. We used  $20 \times 20 \times 15\ \text{mm}^3$  large NdFeB cubes placed in such a way that their magnetization direction (along the 15 mm edge) was parallel to the  $z$ -axis. When mounted, the magnets covered the spanwise range  $-7.5\ \text{mm} \leq z \leq 7.5\ \text{mm}$ . The purpose of this arrangement is to generate a Lorentz force density  $\mathbf{f}$

$$\mathbf{f} = \mathbf{j} \times \mathbf{B} \quad (2)$$

mainly oriented parallel to the  $x$ -axis as in the copper electrolysis experiments described in [51]. Since the current density  $\mathbf{j}$  can be assumed as approximately uniform and parallel to  $y$ , the Lorentz force density is at maximum directly at the electrode and decays rapidly with increasing distance as the  $z$ -component of the magnetic induction  $\mathbf{B}$ . We limit the discussion to a few selected configurations with an upwards directed Lorentz force since this seems to be the logical approach to increase the flow velocity in the electrode gap and thereby decrease the overall void fraction and the effective resistivity for the undivided vertical electrodes. However, we like to stress that it is easily possible to reverse the direction of the liquid flow with a Lorentz force

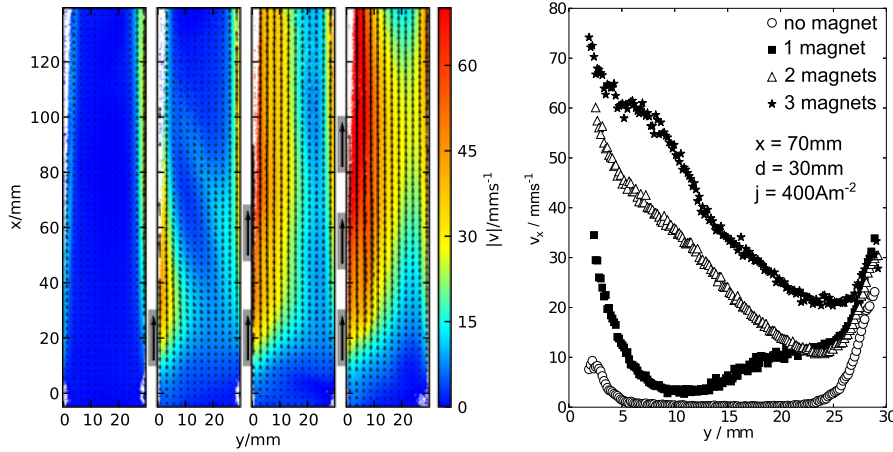


**Fig. 6.** Liquid mean velocity contours with sketched magnet configurations (left). Mean  $v_x$  velocity in a section (right), magnet configurations as on the left. Parameters and position as annotated.

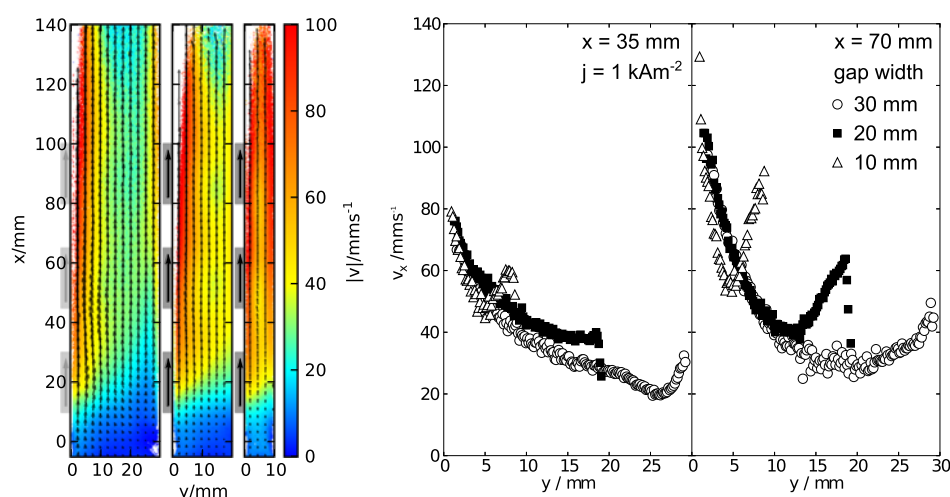
pointing downwards (not shown). This demonstrates that the Lorentz force generated by the cell current and magnetic fields from suitably placed permanent magnets allows for a very flexible design of the liquid flow field, which may be of interest in the case of divided electrodes, where bubbles can be directly moved to the electrodes back side.

Figure 6 shows the liquid velocity distribution in a  $d = 30 \text{ mm}$  wide electrode gap at  $j = 400 \text{ A m}^{-2}$ . Even one magnet extending from  $10 \text{ mm} \leq x \leq 30 \text{ mm}$  brings about a considerable acceleration of the cathode near flow compared to the baseline case. This effect is still clearly visible at a height of  $70 \text{ mm}$ , i.e. two times the magnet's edge length above the magnet. But not only the cathode near flow is changed. While most of the bulk electrolyte of the baseline flow is stagnant, the Lorentz force leads to a positive  $v_x$  velocity over the whole gap width. Adding a second magnet at  $48 \text{ mm} \leq x \leq 68 \text{ mm}$  leads to a further acceleration of the electrolyte flow. Since the second magnet ends just  $2 \text{ mm}$  below the position corresponding to the section on the right of Fig. 6, the shaping effect of the Lorentz force distribution on the  $v_x$  velocity profile is still directly visible over a wide  $y$ -range. Adding a third magnet at  $60 \text{ mm} \leq x \leq 80 \text{ mm}$  while moving the second magnet  $3 \text{ mm}$  downwards results in even larger velocities, mainly in the upper region of the cell.

Keeping the three magnets at their last described positions and increasing the current density to  $j = 1 \text{ kA m}^{-2}$  leads to the velocity distribution shown on the left of Fig. 7. The figure demonstrates the influence of the gap width. Due to the higher Lorentz force generated by the larger current density, overall velocities at  $d = 30 \text{ mm}$  are increased compared to Fig. 6. In the contour plots for the gap width of  $d = 20 \text{ mm}$ , regions of slightly decelerated flow can be seen near the anode opposite the second and third magnet. While the flow near both electrodes constantly gains velocity, the strong acceleration in the fields of the permanent magnets probably causes this localized effect by enforcing a redistribution of the mass flow. For a better understanding, in addition to the in-plane flow field, information about  $v_z$  would be needed. As sketched in Fig. 1, the cell is open to the sides so that fluid can enter and leave the electrode gap also in  $z$ -direction.

With decreasing gap width the average Lorentz force density in the electrode gap increases and so does the average flow speed. While the differences are minor in the lower cell part ( $x = 35 \text{ mm}$ , middle diagram of Fig. 7), they can be clearly seen for





**Fig. 7.** Influence of the gap width  $d$  on the liquid mean velocity (left). Mean  $v_x$  velocity in two sections (middle, right). Three magnets behind the cathode. Parameters and position as annotated.

$x = 70$  mm. Note that the gas evolved at the electrodes generates distinct velocity maxima even for the smallest gap width investigated here.

## 4 Conclusions

Outflow boundary conditions can have a huge influence on the flow in a relatively large part of the electrolytic cell. The flow in a bubble curtain undergoes transition with characteristic features comparable to those observed in single phase wall jets. Lorentz forces originating from permanent magnets are a flexible tool to shape the flow field in the electrode gap.

Financial support from Deutsche Forschungsgemeinschaft (DFG) in frame of the Collaborative Research Center SFB 609 is gratefully acknowledged.

## References

1. D. Pletcher, X. Li, *Int. J. Hydrogen Energy* **36**, 15089 (2011)
2. D. Sauer, *Solarzeitalter* **18**, 12 (2006)
3. F. Hine, M. Yasuda, R. Nakamura, T. Noda, *J. Electrochem. Soc.* **122**, 1185 (1975)
4. F. Hine, K. Murakami, *J. Electrochem. Soc.* **127**, 292 (1980)
5. H. Vogt, in *Electrodics: Transport*, edited by E. Yeager, J. Bockris, B. Conway, S. Sarangapani (Plenum Press, New York and London, 1983), vol. 6 of *Comprehensive Treatise of Electrochemistry*, p. 445
6. J. Maxwell, *A Treatise on Electricity and Magnetism*, vol. 1 (Clarendon Press, Oxford, 1873)
7. G. Kreysa, M. Kuhn, *J. Appl. Electrochem.* **15**, 517 (1985)
8. F. Hine, M. Yasuda, Y. Ogata, K. Hara, *J. Electrochem. Soc.* **131**, 83 (1984)
9. Y. Nishiki, K. Aoki, K. Tokuda, H. Matsuda, *J. Appl. Electrochem.* **17**, 67 (1987)
10. J. Jorne, J. Louvar, *J. Electrochem. Soc.* **127**, 298 (1980)
11. L. Janssen, J. Geraets, E. Barendrecht, S. van Stralen, *Electrochimica Acta* **27**, 1207 (1982)

12. B. Bongenaar-Schlenter, E. Barendrecht, L. Janssen, S. van Stralen, in *Dechema-Monographien*, vol. 98 (Verlag Chemie, 1985), p. 445
13. Y. Nishiki, S. Nakamatsu, K. Aoki, K. Tokuda, J. Appl. Electrochem. **19**, 90 (1989)
14. M. Kuhn, G. Kreysa, J. Appl. Electrochem. **19**, 720 (1989)
15. C.W.M.P. Sillen, Ph.D. thesis, TU Eindhoven, 1983
16. B. Bongenaar-Schlenter, L. Janssen, S. van Stralen, E. Barendrecht, J. Appl. Electrochem. **15**, 537 (1985)
17. J. Eigeldinger, H. Vogt, Electrochimica Acta **45**, 4449 (2000)
18. B. Balzer, H. Vogt, J. Electrochem. Soc. **150**, E11 (2003)
19. M. Kuhn, G. Kreysa, J. Appl. Electrochem. **19**, 677 (1989)
20. Y. Fukunaka, K. Suzuki, A. Ueda, Y. Kondo, J. Electrochem. Soc. **136**, 1002 (1989)
21. P. Boissonneau, P. Byrne, J. Appl. Electrochem. **30**, 767 (2000)
22. I. Kuroda, A. Sakakibara, T. Sasaki, Y. Murai, N. Nagai, F. Yamamoto, Jpn. J. Multiphase Flow **22**, 161 (2008)
23. L. Sigrist, Ph.D. thesis, ETH Zürich, 1978
24. H. Riegel, J. Mitrovic, K. Stephan, J. Appl. Electrochem. **28**, 10 (1998)
25. H. Vogt, Physicochem. Hydrodyn. **8**, 373 (1987)
26. H. Vogt, J. Appl. Electrochem. **29**, 1155 (1999)
27. A. Dahlkild, J. Fluid Mech. **428**, 249 (2001)
28. M. Mat, K. Aldas, O. Ilegbusi, Int. J. Hydrogen Energy **29**, 1015 (2004)
29. M. Mat, K. Aldas, Int. J. Hydrogen Energy **30**, 411 (2005)
30. K. Aldas, N. Pehlivanoglu, M.M.D., Int. J. Hydrogen Energy **33**, 3668 (2008)
31. P. Mandin, J. Hamburger, S. Bessou, G. Picard, Electrochimica Acta **51**, 1140 (2005)
32. A. Alexiadis, M. Dudukovic, P. Ramachandran, A. Cornell, J. Wanngård, A. Bokkers, Chem. Eng. Sci. **66**, 2252 (2011)
33. A. Alexiadis, M. Dudukovic, P. Ramachandran, A. Cornell, J. Appl. Electrochem. **42**, 679 (2012)
34. A. Alexiadis, M. Dudukovic, P. Ramachandran, A. Cornell, J. Wanngård, A. Bokkers, Theor. Comput. Fluid Dyn. **26**, 551 (2012)
35. T. Weier, J. Hüller, G. Gerbeth, in *Annu. Rep. Institute of Safety Research*, edited by F.P. Weiß, U. Rindelhardt (Forschungszentrum Rossendorf, 2001), p. 81
36. T. Iida, H. Matsushima, Y. Fukunaka, J. Electrochem. Soc. **154**, E112 (2007)
37. Z. Diao, P. Dunne, G. Zangari, J. Coey, Electrochem. Comm. **11**, 740 (2009)
38. H. Matsushima, D. Kiuchi, Y. Fukunaka, Electrochimica Acta **54**, 5858 (2009)
39. H. Matsushima, T. Iida, Y. Fukunaka, J. Solid State Electrochem. **16**, 617 (2012)
40. H. Matsushima, T. Iida, Y. Fukunaka, Electrochimica Acta (2012) (in press)
41. M.Y. Lin, L.W. Hourng, C.W. Kuo, Int. J. Hydrogen Energy **37**, 1311 (2012)
42. J. Koza, M. Uhlemann, A. Gebert, L. Schultz, Electrochem. Comm. **10**, 1330 (2008)
43. J. Koza, S. Mühlenhoff, M. Uhlemann, K. Eckert, A. Gebert, L. Schultz, Electrochem. Comm. **11**, 425 (2009)
44. J. Koza, S. Mühlenhoff, P. Żabiński, P. Nikrityuk, K. Eckert, M. Uhlemann, A. Gebert, T. Weier, L. Schultz, S. Odenbach, Electrochimica Acta **56**, 2665 (2011)
45. D. Fernández, M. Martine, A. Meagher, M. Möbius, J. Coey, Electrochem. Comm. **18**, 28 (2012)
46. S. Marini, P. Salvi, P. Nelli, R. Pesenti, M. Villa, M. Berrettoni, G. Zangari, Y. Kiros, Electrochimica Acta **82**, 384 (2012)
47. A. Shah, J. Jorne, J. Electrochem. Soc. **136**, 144 (1989)
48. A. Alexiadis, M. Dudukovic, P. Ramachandran, A. Cornell, J. Wanngård, A. Bokkers, Int. J. Chem. Eng. 392613 (2012)
49. M. Zhou, J. Rothstein, I. Wygnanski, *On the hydrodynamic instability of the wall jet*, in *Proc. 11<sup>th</sup> Australasian Fluid Mechanics Conference* (University of Tasmania, Hobart, Tasmania, 1992), p. 407
50. C. Sillen, E. Barendrecht, L. Janssen, S. van Stralen, Int. J. Hydrogen Energy **7**, 577 (1982)
51. T. Weier, J. Hüller, G. Gerbeth, F.P. Weiss, Chem. Eng. Sci. **60**, 293 (2005)